SANDIA REPORT

SAND2012-4474
Unlimited Release
Printed May 2012

Porosity in Millimeter-Scale Welds of Stainless Steel: Three-Dimensional Characterization

Jonathan D. Madison, Larry K. Aagesen

Prepared by
Sandia National Laboratories
Albuquerque, New Mexico 87185 and Livermore, California 94550

Sandia National Laboratories is a multi-program laboratory managed and operated by Sandia Corporation,
a wholly owned subsidiary of Lockheed Martin Corporation, for the U.S. Department of Energy's
National Nuclear Security Administration under contract DE-AC04-94AL85000.

Issued by Sandia National Laboratories, operated for the United States Department of Energy by Sandia Corporation.

Available to DOE and DOE contractors from
U.S. Department of Energy
Office of Scientific and Technical Information
P.O. Box 62
Oak Ridge, TN 37831

Telephone: (865) 576-8401
Facsimile: (865) 576-5728
E-Mail: reports@adonis.osti.gov
Online ordering: http://www.osti.gov/bridge

Available to the public from
U.S. Department of Commerce
National Technical Information Service
5285 Port Royal Rd.
Springfield, VA 22161

Telephone: (800) 553-6847
Facsimile: (703) 605-6900
E-Mail: orders@ntis.fedworld.gov
Online order: http://www.ntis.gov/help/ordermethods.asp?loc=7-4-0#online

SAND2012-4474
Unlimited Release
Printed May 2012

Porosity in Millimeter-Scale Welds of Stainless Steel: Three-Dimensional Characterization

Jonathan D. Madison
1814 Computational Materials Science & Engineering
Sandia National Laboratories
P.O. Box 5800
Albuquerque, NM 87185-1411

Larry K. Aagesen
Materials Science & Engineering
University of Michigan
2300 Hayward Street
Ann Arbor, MI 48109

Abstract

A variety of edge joints utilizing a continuous wave Nd:YAG laser have been produced and examined in a 304-L stainless steel to advance fundamental understanding of the linkage between processing and resultant microstructure in high-rate solidification events. Acquisition of three-dimensional reconstructions via micro-computed tomography combined with traditional metallography has allowed for qualitative and quantitative characterization of weld joints in a material system of wide use and broad applicability. The presence, variability and distribution of porosity, has been examined for average values, spatial distributions and morphology and then related back to fundamental processing parameters such as weld speed, weld power and laser focal length.

ACKNOWLEDGMENTS

Funding for this project was provided by the Early Career Laboratory Directed Research & Development (EC LDRD) under project award 150638. The authors would also like to thank many individuals at Sandia National Laboratories for their efforts in this work, including Danny MacCallum (Org. 1831) for fabrication of all laser welds, Alice Kilgo (Org. 1822) for metallographic preparation, imaging and micro-indentation, Elizabeth Huffman (Org. 1822) for additional micro-indentation work as well as Burke Kernen and Ciji Nelson (Org. 1522) for micro-computed tomography. The authors also have appreciated very useful conversations with Charles V. Robino (Org. 1831), Brad Boyce (Org. 1831), Jerome Norris (Org. 2552), James Foulk, III (Org. 8256), John Emery (Org. 1524) and Corbett Battaile (Org. 1814). Use of the interfacial shape distribution and interfacial normal distribution analyses developed by P. Voorhees et al. (Northwestern University) are gratefully acknowledged as well.

CONTENTS

FIGURES

TABLES

NOMENCLATURE

CW	Continuous Wave
PW	Pulsed Wave
LBW	Laser Beam Welding
Nd:YAG	Neodymium-doped Yttrium Aluminum Garnet
D/W	Depth-to-Width Aspect Ratio
SW/DW	Surface Width to Depth Width Ratio
μCT	Micro-Computed Tomography
DoE	Department of Energy
NNSA	National Nuclear Security Administration
IDL®	Interactive Data Language by EXELIS Visual Information Solutions

1. INTRODUCTION

It is fundamentally understood that processing determines a materials microstructure and that microstructure; in turn, dictates mechanical response. In practice however, it is rather difficult to quantitatively predict microstructure based primarily upon processing inputs. Laser welds are no exception to this trend. As such, common engineering practice for the qualification and interrogation of welds are generally carried out by post-mortem failure investigations,[1] radiography,[2] and in some cases ultrasonic scans[3]. In practice, these techniques have primarily yielded failure strength values, planar evaluations or two-dimensional projections, of a three-dimensional space. This work, seeks to provide two items; 1) a detailed, three-dimensional quantitative interrogation of millimeter-scale weld microstructures within a window of weld schedules common to a widely utilized material system, and 2) relate resultant microstructure, with chief emphasis on porosity, to the processing parameters of that weld schedule window.

Sandia has long been invested in the development and qualification of welds and brazes used throughout the Department of Energy (DoE) / National Nuclear Security Administration (NNSA). The applications for such joinings span from nuclear weapons and energy to waste storage and even renewable energy technologies. With regard to laser beam welding (LBW) in general, Sandia's efforts can be traced back to at least the early nineties[4] where fundamental processes and the advantages of utilizing high power-density material interactions over very controlled areas were being explored and optimized for manufacturing applications. Later work[5] focused on providing understanding and corrective measures for related effects of laser welding, such as shape distortions. By the mid-2000's Sandia began integrating modeling heavily into investigations to more accurately determine the fundamental heat :: material interaction over a variety of laser and GTA welding processes[6-10]. While not an exhaustive list, the aforementioned do highlight the progression of Sandia's publicly available work in the field.

The work reported here, is a continuation of Sandia's efforts in the investigation of welds, weld processing and weld microstructures. While particulars of this report may be found applicable in the fine-tuning of laser processing parameters, details of the characterization work could also yield useful details to aid in the development of more accurate microstructural models. However, primarily, the focus of this study has chiefly been to enhance the qualitative understanding of microstructures within millimeter-scale laser welds and quantitatively relate the microstructures observed with the processing parameters associated with their formation. While it is recognized that in 304L stainless steels, typical weld parameters for many millimeter scale weldments in operation seek penetration depths on the order of 0.025 – 0.040 in. and are machined with powers in the range of 300 – 500W at 60 – 80 in/min, a weld matrix encompassing a broader range of weld powers and speeds has been selected to increase the overall usefulness of this study. The full details of the weld matrix and sample quantity associated with each intersection of parameters are outlined in detail in Section 3.

2. BACKGROUND

2.1. Porosity

2.1.1. Porosity Formation

While the field has benefited from significant investigations to further understand and model heat :: material interaction among high power density laser welds [9,11-13], a portion of these investigations have focused specifically on the formation of porosity and its driving forces. Among these works, prevailing hypotheses assert that porosity seen in laser welds largely results from intermittent molten pool collapse brought about by a fluctuating imbalance between ablation recoil pressure, molten liquid surface tension and impacting pressure [14-17]. This phenomenon is chiefly referred to as "key-hole collapse" due to the breakdown of a narrow, high aspect ratio, cone-shaped vapor cavity circumferentially bound by molten material. While models have advanced greatly in the incorporation of multi-physics approaches to better understand this weld process, the ability of these models to qualify and specifically predict large-scale microstructure over a broad range of process-parameter space requires further development.

2.1.2. Porosity Effects

Generally, the absence of material encased within a solid body serves to degrade the strength or act as a site in which failure is often linked to as an initiation or propagation site. Furthermore, while highly variable with material type, there typically exists a negative correlation with increases in porosity content and properties such as strength, modulus, hardness, fatigue life, etc. However, the full effect of porosity in 304L stainless steel has not been shown to follow this correlation for all material properties, and as such, its behavior in this regard is not completely understood. The following are two examples in the literature that demonstrate the ambiguity that challenges intuitive understanding in this regard of the effects of porosity in this material.

Boyce, Reu and Robino[1] investigated the mechanical tensile response of autogenous laser welds of 304L stainless steel under two separate weld schedules: continuous wave (CW) and pulsed wave (PW) producing partial-penetration welds nominally 500 μm in depth. Readily identifiable root porosity was observed only in the PW case. Boyce and co-authors reported higher yield strengths (Y.S.) in the weldments of both the PW and CW but equivalent ultimate strengths in comparison to their base metals and attributed the increase in Y.S. to a combination of the Hall-Petch effect and ferrite strengthening. Boyce *et al.* also report no decrease in mechanical strength with the presence of porosity. It should be mentioned however, that beyond a pulsed wave and continuous wave mode, notable differences between weld schedules also included an average delivered power roughly 4 times greater than its counterpart and a travel speed approximately 6 times greater in the CW weld with respect to its PW counterpart. Additionally, while not previously observed and reported, smaller-scale porosity was found to exist in the CW case through utilization of the approach that will be outlined in this report. These factors suggest the microstructural arrangement of porosity in these welds was likely more complex than initially believed. Results of porosity content in the aforementioned weld schedules along with a more thorough discussion of the associated implications for previous observations will be provided in Section 5

Kuo and Jeng[18] reported changes in hardness, percent elongation and tensile strength as functions of porosity content in 304L stainless steel and Inconel 690. The amount of porosity content was instantiated through use of multiple pulsed wave (PW) laser welding schedules and one continuous wave (CW) laser-welding schedule. In their design of experiment, the CW weld demonstrated the greatest amounts of porosity in both the 304L and Inconel 690 alloys. For the Inconel alloy, all increases in porosity were matched with significant reductions in hardness, percent elongation and tensile strength. In the case of 304L, increases in porosity were accompanied by notable decreases in hardness, but no significant variation in percent elongation and very minimal changes in yield strength. Specifically, decreases in tensile strength across increasing porosity content within pulsed wave welds were identified but the CW weld which contained the greatest amount of porosity demonstrated a tensile strength slightly greater than all its PW counterparts. This suggests that when all process parameters remain unchanged, porosity can be a moderate measure for decreases in hardness and tensile strength; however, transitioning between CW and PW laser welding may introduce microstructural variation that adjusts or exceeds the singular effect of porosity in 304L.

2.1.3. Porosity Mitigation

While the full scope of porosity effects in laser welds of 304L stainless steel have yet to be completely ascertained, it has been shown that porosity poses deleterious effects of varying degree, to the mechanical properties and performance of most metallic systems. Some examples of porosity's effect in other systems include: 1) documented losses in hardness in the vicinity of welded regions of austenitic stainless steels[19], 2) greater influence in the reduction of fatigue life when compared to thermal environment in cast aluminum alloys[20], 3) increasing amounts of in-service creep and reductions to overall corrosion resistance in stainless steels based on trapped gases within pores[21]. As a result, the general philosophy associated with handling porosity across nearly all processed metallic systems has been suppression and/or elimination when possible. In laser welds this is accomplished in a variety of ways. Haboudou *et al.* found that varying surface preparation and/or the use of a dual beam configuration helped reduce the presence of porosity in LBW of aluminum alloys[2]. Kuo and Jeng also supported these findings by documenting specific pulsed wave configurations which demonstrated marked decreases in porosity content directly correlated with the change in power delivered to the weld between subsequent pulses[18]. Furthermore, Norris *et al.* showed increasing spot size[22], utilizing longer focal lengths, increasing travel speed and the use of specific shielding gases all served to either reduce the size of, or eliminate the presence of porosity altogether[23].

2.2. Three-Dimensional Reconstructions & Characterization

2.2.1. Progression of Three-Dimensional Techniques in Materials Science

Three-dimensional reconstructions have been instrumental in yielding new findings and producing fresh insights among materials investigations. As an abbreviated and cursory listing, the authors offer the following examples.

In the mid nineties, Mangan and Shiflet performed serial-sectioning experiments of pearlite colonies in high manganese containing steels and discovered ferrite and cementite lamellae exist in constant contact with austenite grains with specific orientations. Conventional two-dimensional observations of the same pearlite colonies suggested intragranular nucleation resulting in isolated cementite islands within grain interiors. Mangan and Shiflet clearly showed the isolated cementite features were actually portions of the same interconnected colony[24,25].

As contemporaries to Mangan and Shiflet, Kral and Spanos also investigated larger volumes of cementite morphologies in steels and were among the first to combine crystallographic measures of precipitates and grain orientation within their reconstructions. A chief contribution of Kral and Spanos' work was the development of one of the first fully developed computer-aided three dimensional reconstruction toolsets for visualizing reconstructions which also allowed for isolation, cropping and subset identification for direct measurements of select regions of a reconstruction. The primary technical contribution of their work was in the identification, visualization and initial measurements of two fundamental types of cementite precipitates; grain boundary and Widmanstätten lathes[26-30].

Beginning in the early 2000's, Voorhees and co-workers began reporting on the development of the first fully automated serial-sectioning system applicable to "softer" metals such as Al-Cu and Pb-Sn. Their contribution was the first instance of a self-contained, fully automated, metallographic serial-sectioning system inclusive of preparation, imaging and closed-loop depth removal measurement. In a few years following, Spowart and Mullens would present a solution for fully automated serial-sectioning across a broader variety of systems including very strong and formidable materials such as nickel-base superalloys, human bone, discontinuously reinforced composites and pitch-based carbon foams[31-36]. Spowart and Mullens would eventually go on to license their process and the system itself would later become commercially available under the trademark name of Robo-MET.3D®[37].

Most recently, Chawla *et al.* and Lewis, *et al.* have independently been instrumental in pioneering image-based microstructural finite element modeling from three-dimensional reconstructed datasets. In the work of Chawla and co-workers, 3D datasets of particle-reinforced composites were digitized and examined for mechanical response under a variety of loading conditions and under varied shape approximations of the imbedded particulates[38,39]. In the work of Lewis and co-workers, statistically relevant populations from very large-scale three-dimensional datasets of polycrystalline titanium and austenitic stainless steels have been obtained through serial-sectioning. This data is combined with grain orientations acquired via electron back-scattered diffraction acquired during serial-sectioning. This addition allows or analysis of grain boundary character, curvature and local and long-range mis-orientations. The reconstruction along with all known crystallographic information is then imported into a finite element domain for investigation of mechanical and material response[40-44]. These works have been pivotal in the development of 3D techniques in materials science as they indicate some of the first efforts to directly import the acquired three-dimensional data into a simulation and modeling domain to illustrate the variation in result caused by performing the same analysis with decreasing accuracy in microstructural features and representative volume elements.

Other recent advances in three-dimensional data-collection methodologies include the automation of focused ion beam (FIB) serial-sectioning by Uchic & DeGraef[45-47], Seidman and other's development of local electron atom-probe for fine-scale three-dimensional reconstructions[48-50], Echlin and Pollock's development of an *in-situ* SEM/FIB/Femtosecond Laser Tri-Beam serial-sectioning system[51,52], as well as non-destructive approaches for three-dimensional data generation including Buffiére and co-authors work in utilizing x-ray or synchrotron radiation tomography[53-55] and Lauridsen and co-authors work in 3D x-ray diffraction (3DXRD)[56-58].

2.2.2. Current State of the Art Three-Dimensional Interrogation Methods

As illustrated in the preceding section, the use of three-dimensional reconstructions and characterization in materials science has experienced tremendous attention, large-scale growth, and unprecedented development within the materials community over the past two decades. This has been largely owed to recent advances in automated data collection[59], advancing segmentation techniques[60-65] and further integration of three-dimensional data within simulation and modeling domains[66]. Approaches for acquiring three-dimensional data exist on varying length scales and are nearly as numerous as the amounts of materials systems investigated as illustrated by the abbreviated list provided in the previous section. it is useful to first consider these methods in terms of their length-scale; and secondly, in terms of their destructive (D) or non-destructive (ND) nature. Table I lists these methods and details their length-scales, destructive or non-destructive nature, relative data acquisition time and associated references. Alternatively, for illustrative purposes, Fig. 1 shows the most common of three-dimensional interrogation methods and the length-scales over which such methods have been demonstrated as practical.

Table I – Three-dimensional data collection methods, associated details and references

	Length-scales (m)	Destructive (D/ND)	Data Acquisition Time	References
Atom Probe Tomography [APT]	$10^{-10} – 10^{-8}$	D	Medium	[48-50, 67]
Focused Ion Beam Milling [FIB]	$10^{-8} – 10^{-5}$	D	Medium	[45-47, 59, 68]
Mechanical Serial-Sectioning [MecSS]	$10^{-7} – 10^{-3}$	D	High	[28, 32, 34, 42, 44, 69]
3DXray Diffraction [3DXRD]	$10^{-6} – 10^{-3}$	ND	High	[56-58]
Micro-Computed Tomography [µCT]	$10^{-6} – 10^{-3}$	ND	Low	[53-55, 70, 71]
Femto-second Laser Sectioning [FSL]	$10^{-5} – 10^{-3}$	D	Low	[51, 52]
Ultrasonic Testing Scan [USTC]	$10^{-5} – 10^{-1}$	ND	Low	[3, 72]

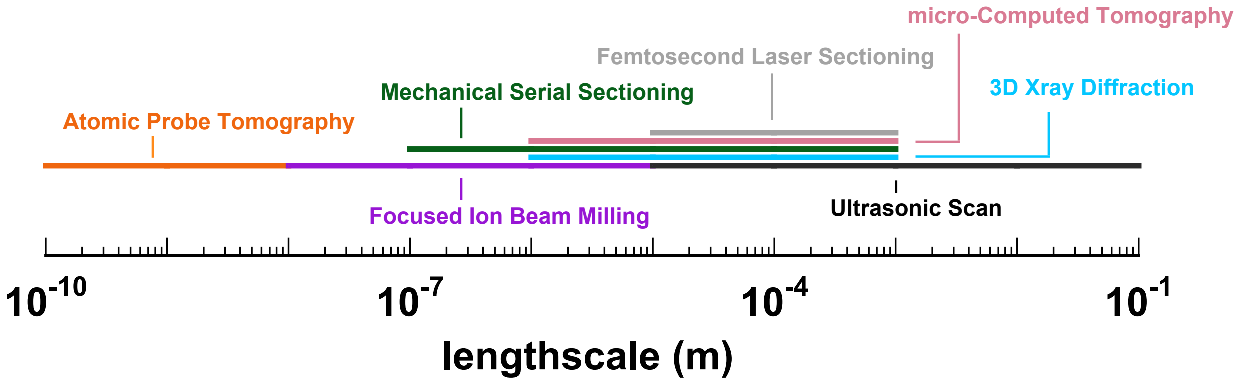

Figure 1 – Three-dimensional data collection tools and their associated length-scales

3. EXPERIMENTAL PROCEDURE

3.1. Nd:YAG CW Laser Welding

A matrix of 36 edge-joint laser welds yielding varied microstructure and differing porosity levels were welded with a flash lamp driven, fiber delivered, ROFIN-Sinar, Inc. continuous wave, 015 HQ, Nd:YAG laser. For each weld, two-2.54 cm x 10.16 cm x 0.1 cm plates of 304L stainless steel having a nominal composition of Fe-0.04C-18.12Cr-1.21Mn-8.09Ni-0.028N-0.022P-0.001S-0.34Si (wt pct) were oriented parallel to one another, fixed at their base by clamp and welded on their upper seam. Power delivered in each set of welds was measured prior to machining via a Macken P2000Y Laser Power Probe. Delivered powers ranging from 200 – 1200 W were used in conjunction with constant travel speeds of 252, 510, 1016, 1524, and 2032 mm/min [or 10, 20, 40, 60 and 80 in./min), respectively. For welds at 1200W, two welds were machined with both an 80 mm and 120 mm focusing lens. This was done to allow for redundant characterization using micro-computed tomography and metallography, among the highest power and the three highest speeds. These samples will be referred to in this study as "redundant" samples. For a matrix view of the full process parameter spaced investigated see Table II.

Table II – Process parameter map detailing edge welds machined in this investigation

[80 mm focal lens]	**252 mm/min**	**510 mm/min**	**1016 mm/min**	**1524 mm/min**	**2032 mm/min**
Delivered Power (W)	**10 in/min**	**20 in/min**	**40 in/min**	**60 in/min**	**80 in/min**
1200			**(2) ×**	**(2) ×**	**(2) ×**
[120 mm focal lens]	**252 mm/min**	**510 mm/min**	**1016 mm/min**	**1524 mm/min**	**2032 mm/min**
Delivered Power (W)	**10 in/min**	**20 in/min**	**40 in/min**	**60 in/min**	**80 in/min**
1200			**(2) ×**	**(2) ×**	**(2) ×**
1000		**(1) ×**	**(1) ×**	**(1) ×**	**(1) ×**
800	**(1) ×**	**(1) ×**	**(1) ×**	**(1) ×**	**(1) ×**
600	**(1) ×**	**(1) ×**	**(1) ×**	**(1) ×**	**(1) ×**
400	**(1) ×**	**(1) ×**	**(1) ×**	**(1) ×**	**(1) ×**
200	**(1) ×**	**(1) ×**	**(1) ×**	**(1) ×**	**(1) ×**

3.2. Micro-Computed Tomography & Metallography

Micro-computed tomography (μCT) was employed for characterization of porosity using a Kevex PSX10-65W x-ray tube operating at 130KV and 250μA. In this arrangement, the sample was rotated counter-clockwise at a speed of 0.12 degrees/sec by a Parker 3-axis stage. Transmitted signals are received on a Varian 2520 cesium iodide fluorescent plate through a magnification lens yielding an effective pixel size. The mid-range voxel (or three-dimensional pixel) resolution of the redundant 80 and 120 mm focal lens sets were 31 and 27 μm^3/voxel, respectively. Higher and lower resolution scans ranging from 9 (μm^3/voxel) to 20 (μm^3/voxel) were employed fro all other weld scans based on coarseness of the porosity present and fidelity required to resolve the features present. Following tomography, one of each of the redundant samples produced at high speed and power were sectioned at three separate intervals along the length of each weld, metallographically prepared and imaged for comparison via optical microscopy.

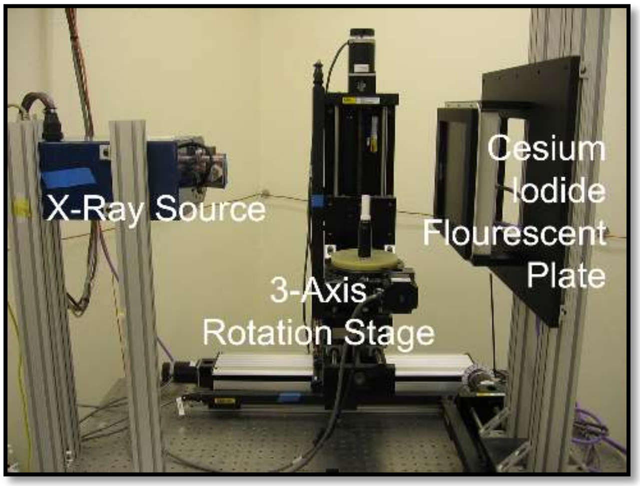

Figure 2 – Micro-Computed Tomography setup at Sandia National Laboratories (Org. 1522)

3.3. Data Reconstruction, Microscopy & Characterization

3.3.1. Segmentation, 3D Reconstruction & Measurement

In an effort to exercise greater control over the acquired data and limit or expand the interrogated volume of interest, some micro-computed tomography data was analyzed in the commercially available VGStudioMax© software while all other data was imported into the Interactive Data Language (IDL®) and evaluated. In order to do this, image segmentation was performed on slice views of the μCT data. Since the μCT data collection occurs over two to three individual scans due to part size, a uniform image slice size is determined which will encompass all features across all slices. Next, each image is made binary by thresholding each slice by a uniform value to provide clear demarcation between the weld metal and the internal pores. Lastly, each image is "cleaned" of any anomalous CT scan artifacts and stacked into an array for visualization in IDL®. It should be noted that all image segmentation not occurring directly in IDL® were performed in Adobe Photoshop CS5©.

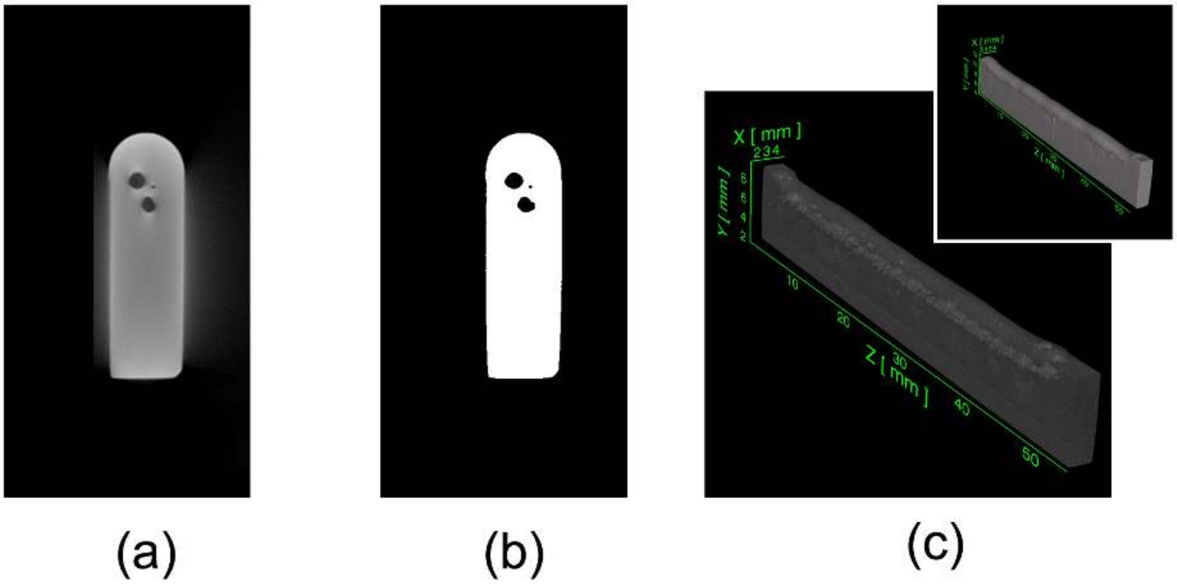

Figure 3 – (a) Non-segmented Micro-Computed Tomography Slice Image (b) Segmented slice and (c) Three-Dimensional Reconstruction in IDL® (upper image displays entire weld sample, lower image displays weld exterior made partially transparent to reveal internal pore structures.

Following visualization, custom programming scripts within IDL® have been developed to allow for measurement of specific details and features including pore volumes, distributions, frequency, shape and orientation in the weld.

3.3.2. Microscopy, Imaging & Measurement

Complimentary to μCT, optical microscopy imaging of the redundant sectioned and metallographically prepared samples were obtained. Images were taken at low magnification (50X) showing the totality of the weld envelope in cross-section and also at high magnification (500X) showing the local microstructure in the base metal, the heat affected zone and the welded ligament. The low magnification images allowed for visual inspection and measurement of macro-scale features across the weld cross-sections. These measurements included; penetration depth, weld width at the joint surface, interior weld width across the joining, crown height, heat affected zone breadth and overall weld envelope. These measures provided opportunity for direct comparison with μCT results and the return of measures not directly obtainable with μCT.

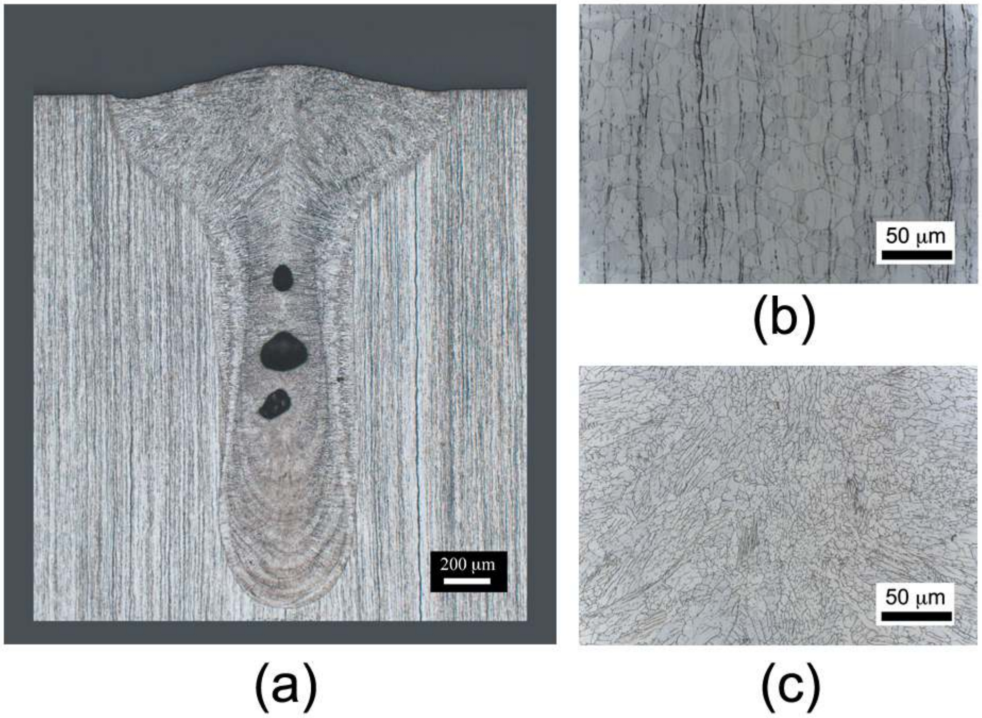

Figure 4 – Optical Microscopy Images of (a) Total Weld Cross-section (b) Microstructure in Base Metal Cross-section (c) Microstructure at Weld Centerline Cross-section

3.4. Micro-Indentation Testing

Lastly, to assess basic variations in material properties of the welded regions and base metal independently, micro-indentation studies were performed on a collection of weld samples. One sample from each of the redundant specimens was selected and micro-indentation was performed. Three separate cross-sections were evaluated per sample. For each cross-section, five to six indents throughout welded region were made followed by five to six more indents in the base metal using a Vicker's tip in a Shimadzu HMV-2000 micro-indenter under a 0.5 kg load. Indents suspected of sampling the heat-affected zone were disregarded from the analysis. The 0.5 kg load was selected to overcome any inherent elastic response in the metal and provide a moderate conversion measure to calculate nominal yield and tensile strengths. Recent relationships developed by Pavlina and Van Tyne[73] to correlate both yield strength and tensile strength in non-austenitic steels with Vicker's hardness measures were appropriated. These relationships are shown below;

$$\text{Y.S.} = -90.7 + 2.876H_V \qquad \text{Eq. 1}$$

$$\text{T.S.} = -99.8 + 3.734\, H_V \qquad \text{Eq. 2}$$

where Y.S. and T.S. are yield strength and tensile strength respectively and H_V is the Vicker's diamond pyramidal hardness, which is returned in units of kg_f/mm2. For the sake of consistency, the values reported here will utilize the same reporting convention. Although 304L is austenitic, the approximate material properties calculated by Eq. 1 and 2 well exceed the minimum ASTM A240 and ASME SA-240 requirements for 304L at room temperature[74] and are in moderate agreement with previously reported experimental values for similarly welded 304L stainless steel[1,18].

4. CHARACTERIZATION RESULTS

4.1. Metallographic Observations

Metallographic cross-sections reveal typical trends in the ratio of penetration depth to weld width[18,23,75-79] with increasing weld speed and focal distance (Table III). As travel speeds or focal distances increase, we would expect a decrease in the depth-to-width ratio resulting from less power penetration into the interior of the part due to faster movement of the laser beam, or increasing losses in the coherence of the beam with increasing distance to the part. Although any loss in coherence is very minor over the distances used in these sets of experiments, the results below suggest focal lens provides a greater adjustment to the overall depth-to-width ratio at a fixed set of parameters than an incremental change in the weld speed. Micrographs illustrating metallographic cross-sections are shown in Figure 5.

Table III – Weld Matrix with Observed D/W Ratios

Focal Lens (mm)	Weld Speed (mm/min)	D/W Ratio
80	1016	1.44
120	1016	1.28
80	1524	1.43
120	1524	1.18
80	2032	1.45
120	2032	1.26

Two findings not often reported in weld characterization, but likely of seminal importance in the physics of the heat :: material interaction, are the ratio of surface width to subsurface breadth as well as variations in crown height. Here, surface width (SW) is identified as the weld width at the weld surface and subsurface breadth or "depth width" (DW) is defined as the maximum observed weld width at distances at or below half the total penetration depth. Crown height is defined as the elevation of the weldment at its centerline relative to the base metal. While the implications of these measures will be discussed later, the variation of these measures with respect to weld speed is shown in Figure 6 for all redundant samples.

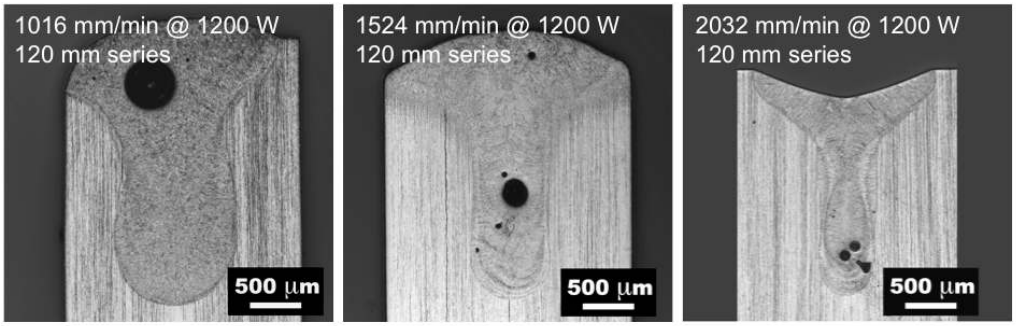

Figure 5 – Metallographic cross-sections of 120 mm weld series at increasing speeds illustrating typical weld shapes, microstructure and embedded pores

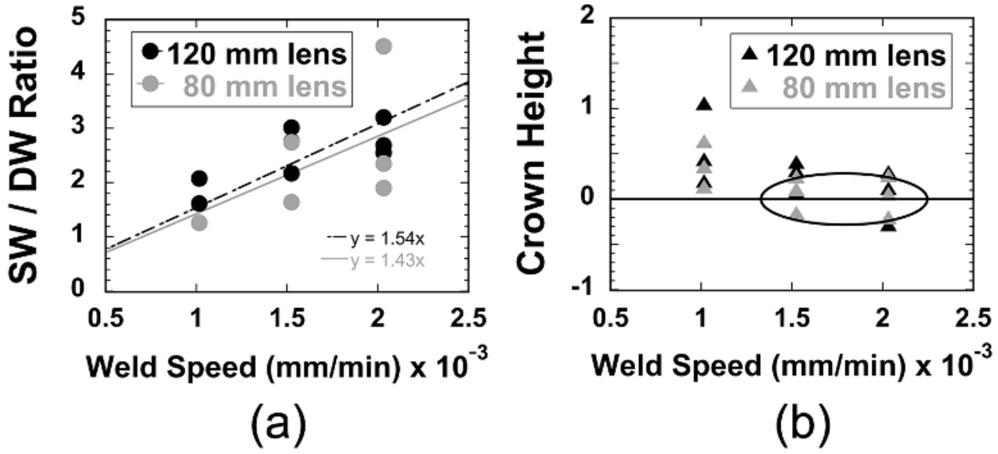

Figure 6 – (a) Surface Width to Depth Width (SW/DW) ratio and (b) Crown Height as functions of weld speed for 80 and 120 mm focal lenses at 1200W delivered power at welding speeds of 1, 1.5, and 2 m/min [40. 60. 80 in/min].

4.2. Micro-Computed Tomographic Analysis

4.2.1. General Observations

Micro-computed tomography revealed trends in porosity size, void distributions, relative location and overall void morphology. To provide a general sense of the presence of porosity as a function of welding parameters, Table IV records whether porosity was observed in each weld, and if so, the maximum pore volume found and the quantity of total pores identified in each weld. To a limit, slower speeds demonstrate a propensity toward larger pores, while higher speeds yield smaller pores with a drastic increase in the quantity present. At very small pore volumes, (e.g. orders of magnitude ≤ 0.009 mm^3) the ability to distinguish all pores declines as the volumes of smaller pores are below the resolution limit of the μCT scan or not present at all. To provide a more thorough analysis of porosity content, the redundant samples which have also been metallographically sectioned, prepared and imaged optically, were also investigated in a more detailed fashion to provide further quantitative analysis of the variations and distributions in size, contribution to total voided space as well as variations in pore shape and pore directionality.

Table IV – General Porosity Content in Expanded Weld Matrix

[80 mm focal lens]	252 mm/min	510 mm/min	1016 mm/min	1524 mm/min	2032 mm/min
Delivered Power (W)	**10 in/min**	**20 in/min**	**40 in/min**	**60 in/min**	**80 in/min**
1200			0.49 mm^3 (373)	0.05 mm^3 (550)	0.03 mm^3 (425)
[120 mm focal lens]	**252 mm/min**	**510 mm/min**	**1016 mm/min**	**1524 mm/min**	**2032 mm/min**
Delivered Power (W)	**10 in/min**	**20 in/min**	**40 in/min**	**60 in/min**	**80 in/min**
1200			0.95 mm^3 (215)	0.10 mm^3 (391)	0.03 mm^3 (736)
1000		1.50 mm^3 (130)	0.51 mm^3 (190)	0.57 mm^3 (381)	0.01 mm^3 (263)
800	0.17 mm^3 (77)	0.59 mm^3 (129)	0.09 mm^3 (302)	0.01 mm^3 (290)	0.006 mm^3 (264)
600	0.24 mm^3 (120)	0.26 mm^3 (284)	0.01 mm^3 (267)	0.007 mm^3 (132)	0.009 mm^3 (91)
400	0.07 mm^3 (81)	0.01 mm^3 (6)	0.001 mm^3 (1)	-- (0)	-- (0)
200	-- (0)	-- (0)	-- (0)	-- (0)	-- (0)

**Maximum Pore Volume Present (Total Quantity of Resolvable Pores)*

4.2.2. Porosity Size and Total Contributions to Voided Space

To further illustrate the measures of average individual void volumes at each redundant weld schedule, minimums of 90% or more of the total voided space in each weld were considered with their associated averages prefixed by the term, "nominal" as displayed in Table V. At both focusing distances, decreases in nominal void volume were apparent, as were increases in nominal voids per unit length, with increases in weld speed, Figure 7.

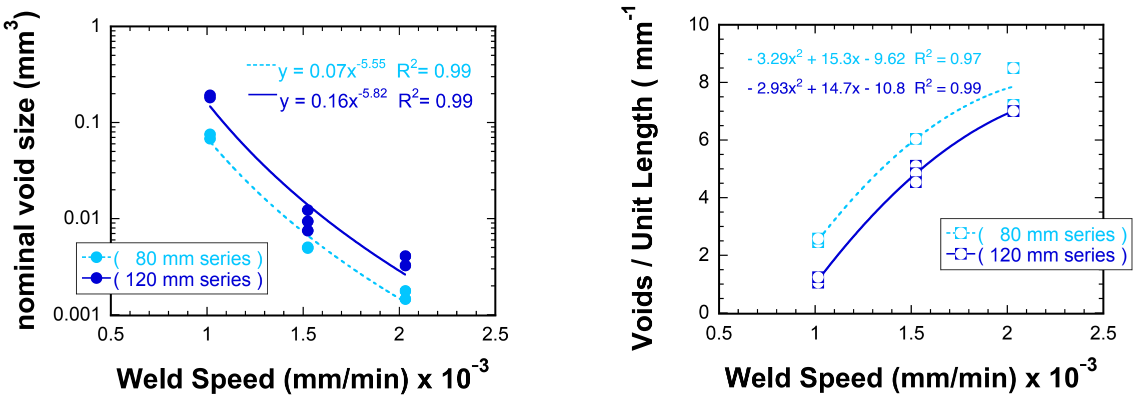

(a) (b)

Figure 7 – (a) Nominal Void size and (b) Voids/Unit Length as functions of weld speed for all redundant weld samples machined at 1200W delivered power for 1, 1.5, and 2 m/min [40, 60, 80 in/min], respectively

It should be pointed out that tomography for the welded samples using the 120 mm lens at 2032 mm/min experienced a change in apparatus that resulted in a minor loss of resolution. Large voids remained distinguishable in size and shape while smaller pores experienced a loss in fidelity. For this reason the voids/unit length is not reported for this sample, Table V. However, beyond average measures, μCT provides for total interrogation of all resolvable internal voids limited only by resolution. As such, a size ordered distribution of all pores among the redundant samples is shown in Figure 8. As can be seen, while separated equidistance in process parameter space (*i.e.* each weld set is separated by the same speed difference of approximately 0.5m/min [or specifically 20 in/min]) the 1 m/min weld series yields maximum porosity sizes an order of magnitude larger in size than its companion welds which both yield nominally equivalent distributions across all sizes detected.

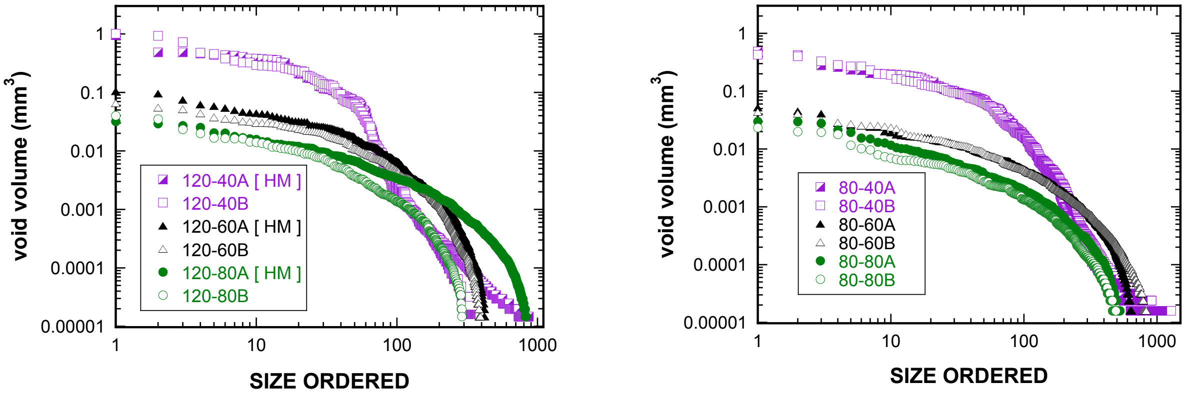

(a) (b)

Figure 8 – Volume Ordered porosity distribution for 80 mm and 120 mm lens series welds at machined at 1200W delivered power for 1, 1.5, and 2 m/min [40, 60, 80 in/min]

To further elucidate the subtle differences among this subset of welds, reconstructions from one weld at each redundant setting are shown in Figures 9 and 10 to illustrate the specifics of the porosity percentage total and size distributions. These findings are consistent with trends and observations provided by Norris *et al.* [22,23,78] but here, physical volumes of the observed porosity are returned, not an observed diameter. Below, porosity histograms, binned by void size (*i.e.* voxels/pore), illustrate that major contributors to the total voided space in each weld are not the most frequently occurring populations, Figures 9 and 10. In fact, voxel bins possessing 10 or fewer voxels/pore contribute less than 7% to the total porosity observed in each case despite being among the most frequently occurring populations. Each histogram pair presented, correspond to the specific reconstruction of pores pictured directly above each set.

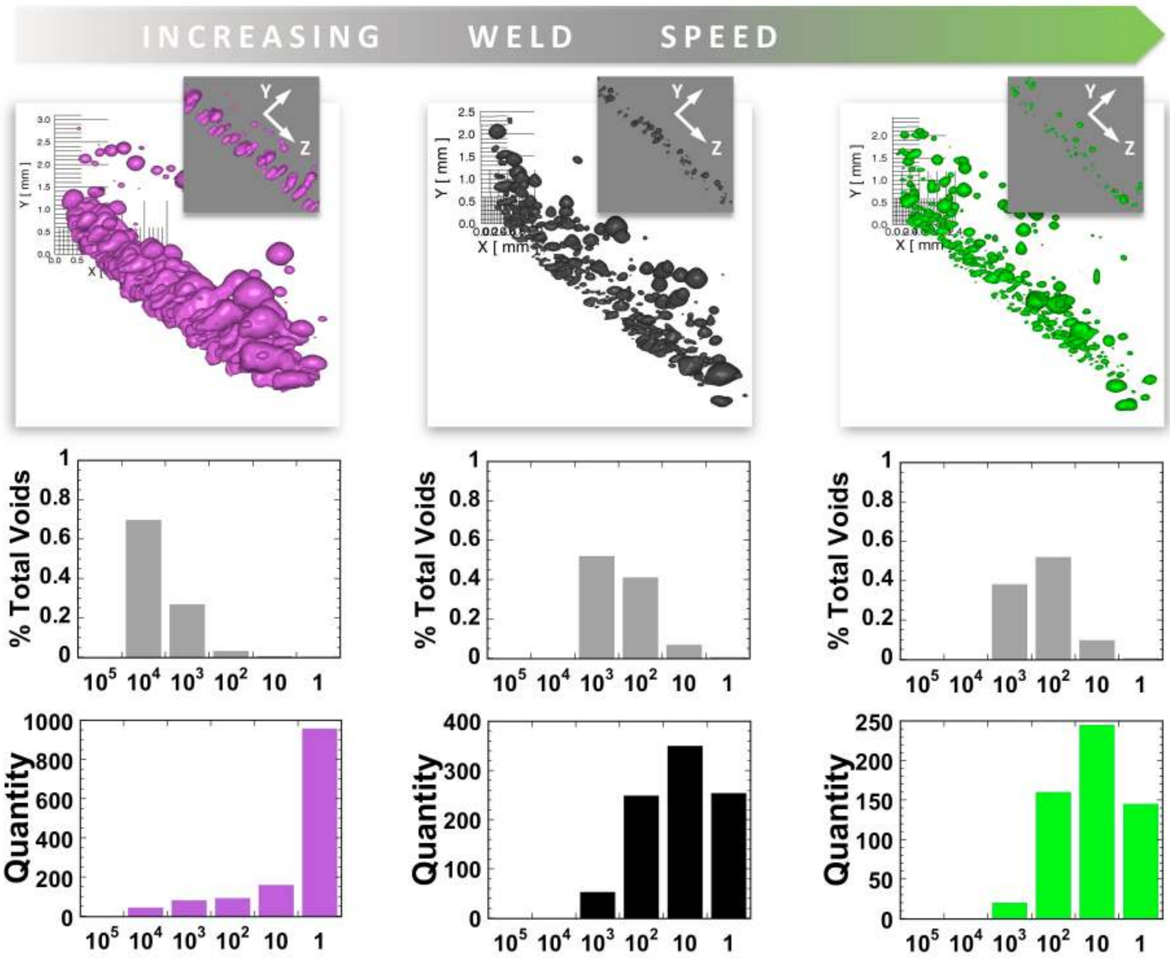

Figure 9 – Micro-CT reconstructions of (a) 80 mm focal lens series at 1200W delivered power for 1, 1.5, and 2 m/min [40, 60, 80 in/min], respectively. Middle series histograms report voided space percentage contributions as functions of voxel size while lower series plots illustrate total quantities of voids in each reconstruction also as functions of voxel size

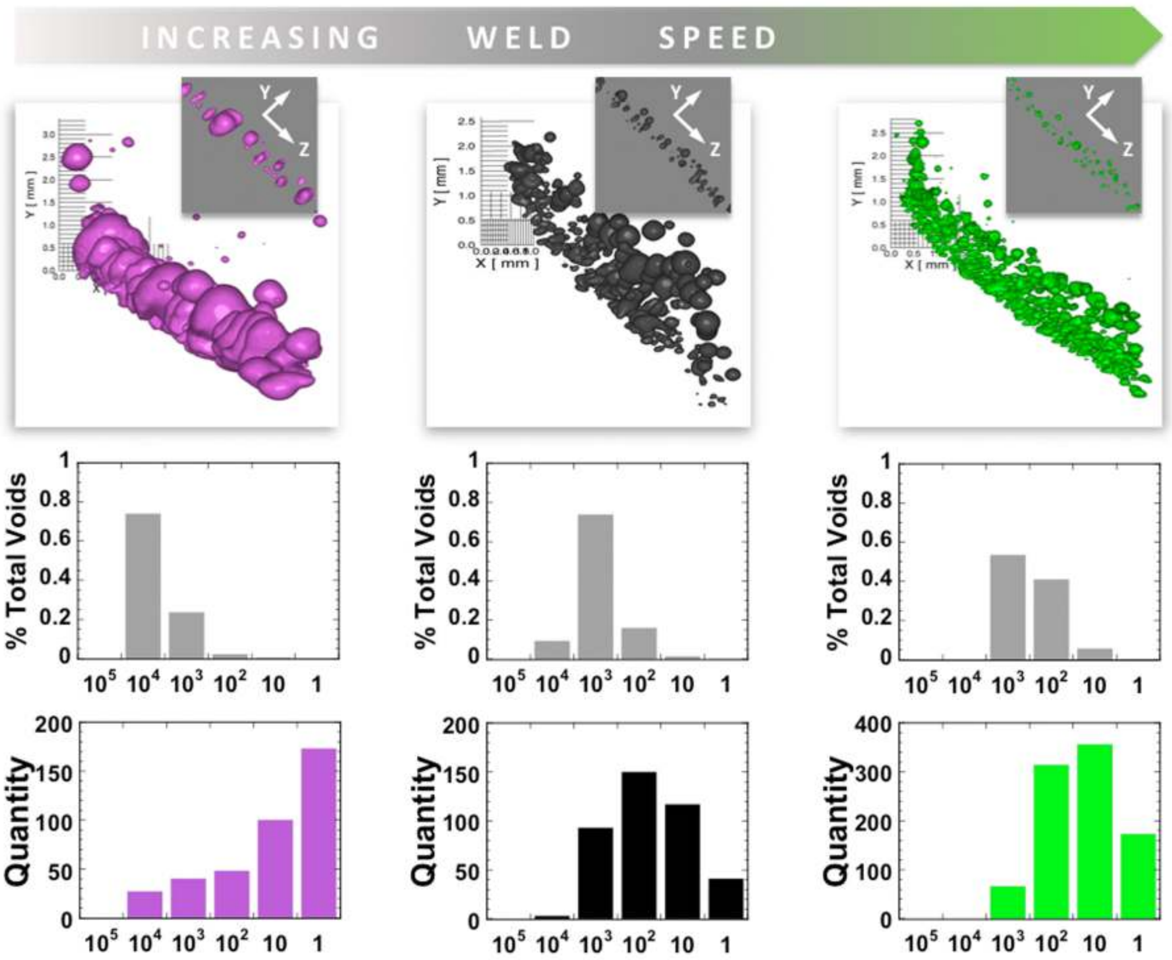

Figure 10 – Micro-CT reconstructions of (a) 120 mm focal lens series at 1200W delivered power for 1, 1.5, and 2 m/min [40, 60, 80 in/min], respectively. Middle series histograms report voided space percentage contributions as functions of voxel size while lower series plots illustrate total quantities of voids in each reconstruction also as functions of voxel size

4.2.3. Porosity Shape

With regards to morphology, Voorhees and co-workers[80-82] have developed methods for describing curvature populations based on principal radii of curvature with primary applications to solidification[83], coarsening in metals[80,82,84,85] and describing topologically complex domains [81,86,87]. One major output of these methods has been interfacial shape distribution (ISD) plots, which indicate the probabilities of encountering an interfacial patch having a specific pairing of principal curvatures. For further details on this method, the reader is referred to the aforementioned references. However, to aid in understanding the visual representation, the ISD legend is illustrated in Figure 11. The authors would like to note; to preclude any confusion, the nomenclature used in the formulation of the ISD legend has not been altered; therefore, in the analysis presented herein, the "S" or "solid" phase corresponds to the weld metal and the "L" or "liquid" phase, in the legend, corresponds to porosity. ISDs for the 80 mm and 120 mm focal lens weld series are shown in Figures 12 and 13 respectively. A uniform scale is used across ISDs of a given focal lens to aid in direct comparison. The units of each scale bar are μm^2 where black corresponds to a quantity of zero and red corresponds to the highest quantity present. In both cases, as weld speeds increase, the ISD population peak shifts from κ_2 nominally equal to 0 with slightly negative values of κ_1, to κ_1 and κ_2 both becoming increasingly negative. This fundamentally means two things; 1) As welding speeds increase, curvature population maxima lose most all κ_2 values greater than 0, indicating a near complete loss of patches that are saddle-like. 2) As welding speeds increase, the morphology of porosity transitions from elliptical with a relatively tight distribution of curvatures to a collection of morphologies more spherical in shape and possessing wider distributions of curvatures owed to increased populations of decreasing void sizes. To make the transition in morphology more clear, ellipses were fit to individual voids in each reconstruction of redundant samples while returning the major (α), minor 1 (β) and minor 2 dimensions of each ellipse for extrapolation of diameter anisotropy. In this measure, a minimum of ninety percent and a maximum of ninety-nine percent of the voided space within each weld were considered. To compare across varying sizes, each pore's α and β axes lengths were normalized by its minor2 diameter. It was found that at slow speeds, pores exhibit a major diameter nearly twice that of its secondary and tertiary axes. While increases in weld speed or focal length decrease shape anisotropy, a 1:1:1 aspect ratio is never reached. Averages and standard deviations for each case of this ellipse fit analysis are recorded in Table IV.

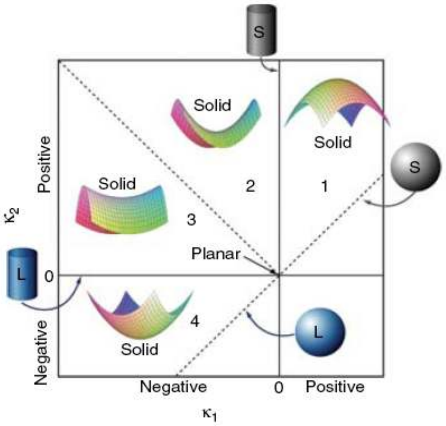

Figure 11 – Interfacial Shape Distribution Legend (reproduced from Mendoza et al. 2003)

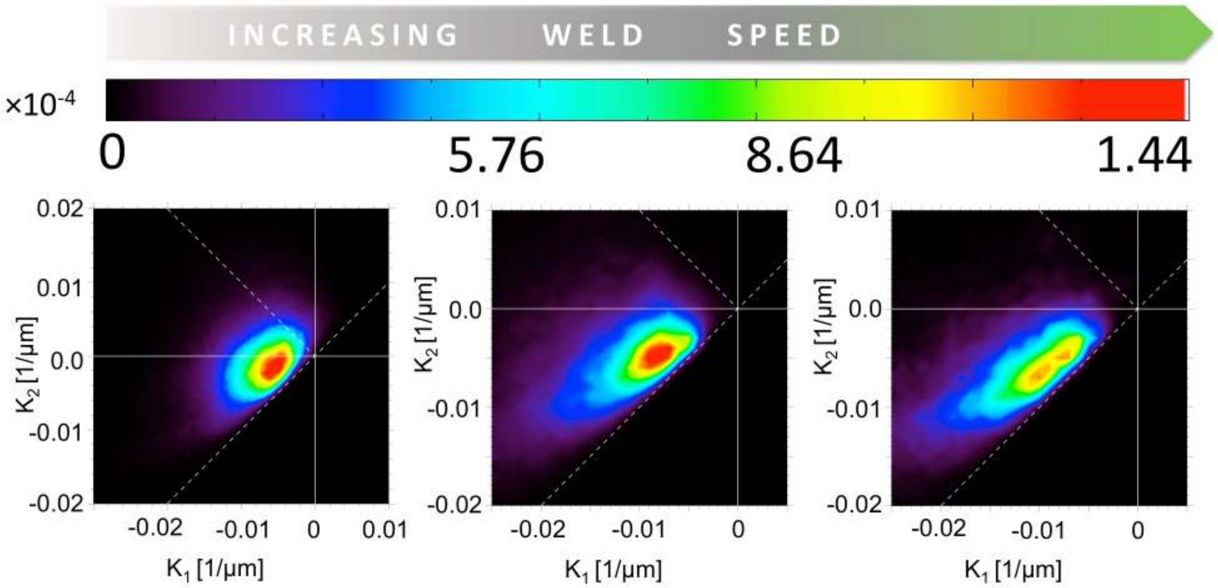

Figure 12 – Interfacial Shape Distribution Plots for 80 mm focal lens weld series machined at 1200W delivered power for 1, 1.5, and 2 m/min [40, 60, 80 in/min]

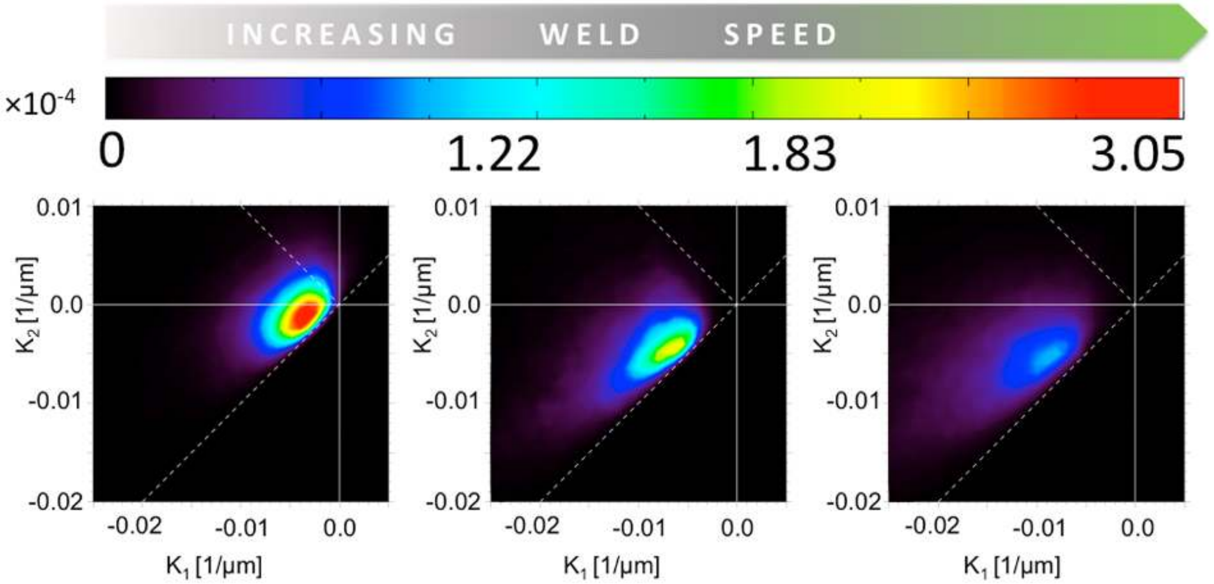

Figure 13 – Interfacial Shape Distribution Plots for 120 mm focal lens weld series machined at 1200W delivered power for 1, 1.5, and 2 m/min [40, 60, 80 in/min]

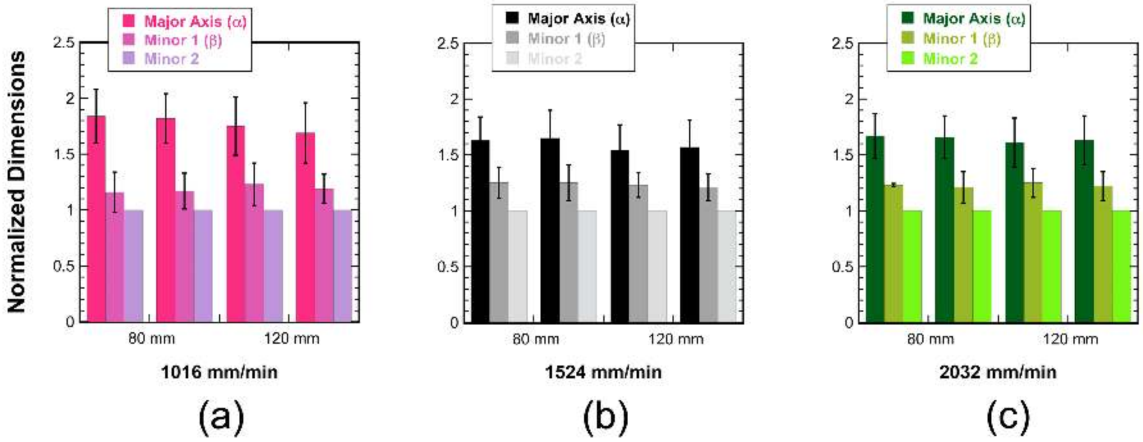

Figure 14 – Average ellipse fit dimensions (normalized to minor 2 axes for all pores)

Table V – Weld Matrix with Observed 3D Characterization Measures

Focal Lens (mm)	Weld Speed (mm/min)	Nominal Void Volume (mm^3)	Nominal Voids/Unit Length (mm^{-1})	Normalized Nominal Shape Anisotropy		
				Major (α)	Minor1 (β)	Minor 2
80	1016	0.075	2.46	1.84 ± 0.24	1.16 ± 0.18	1
80	1016	0.068	2.58	1.82 ± 0.22	1.17 ± 0.16	1
120	1016	0.190	1.05	1.75 ± 0.26	1.23 ± 0.19	1
120	1016	0.180	1.24	1.69 ± 0.27	1.19 ± 0.13	1
80	1524	0.0050	6.04	1.63 ± 0.21	1.25 ± 0.14	1
80	1524	0.0049	6.04	1.65 ± 0.25	1.25 ± 0.16	1
120	1524	0.0094	5.11	1.54 ± 0.23	1.23 ± 0.11	1
120	1524	0.0075	4.54	1.57 ± 0.24	1.21 ± 0.12	1
80	2032	0.0018	8.50	1.67 ± 0.20	1.23 ± 0.14	1
80	2032	0.0015	7.22	1.66 ± 0.19	1.21 ± 0.14	1
120	2032	0.0032	7.01	1.61 ± 0.22	1.25 ± 0.13	1
120	2032	0.0041	--	1.63 ± 0.22	1.22 ± 0.13	1

4.2.4. Porosity Directionality

Another product yielded by the work of Voorhees and co-workers which is complementary in nature to the ISD, is the interfacial normal distribution or (IND)[81,88]. This data representation illustrates the relative preferred directionality in a microstructure. In this work, we only employ equal area projections along the z direction with the projection plane being the x-y plane of each reconstruction as illustrated in Figures 9 and 10. This plane is normal to the welding direction and the recipient of the majority of the observed interfacial normals. To assist the reader in interpreting the INDs presented here, a schematic illustration of the IND projection is shown in Figure 15. Furthermore, to scope the extremes of an IND representation, the reader could imagine an observer witnessing the IND for a perfectly smooth plane oriented parallel to the projection plane and an IND for a perfectly smooth sphere. The IND for the plane would simply be a point as all normals project to the same point in space on the equal-area projection plane. Conversely, the IND for the sphere would reveal an equal population of normals at all locations across the projection plane as there are theoretically a equivalent amount of normals pointing outward for every patch of surface on the sphere. Succinctly stated, the lower the curvature of the object, the more focused the IND spread and alternatively, the greater the curvature, the larger the spread. Below, Figure 15 demonstrates the IND projection of a single point on a reference sphere. Note: the (x,y,z) reference axis illustrated in Figure 15 is arbitrary and not related to the visualization of porosity shown elsewhere in this work.

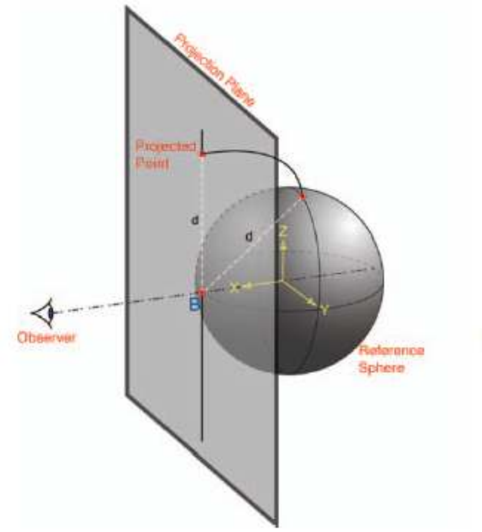

Figure 15 – Schematic illustration of the Interfacial Normal Distribution for an equal area projection (reproduced in part from Kammers, 2006)

Figures 16 and 17 show the Interfacial Normal Distributions for the 80 mm and 120 mm reconstructions illustrated prior in Figures 9 and 10 and whose ISDs are reported in Figures 12 and 13, respectively. In consistency with the ISDs, the color bar atop each plot indicates the relative populations present where black indicates a population of zero and red indicates the highest quantity present. Each image possesses it own scale bar to help elucidate features which would be washed out with a uniform scaling. As can be observed, with increases in weld speed, both weld series demonstrate increased curvature and decreasing specific directionality. This shows the porosity produced in the slower welds have relatively higher directionality than their counterparts. This further supports the observation of near elliptical pores transitioning to more spherical geometries with increases in travel speed.

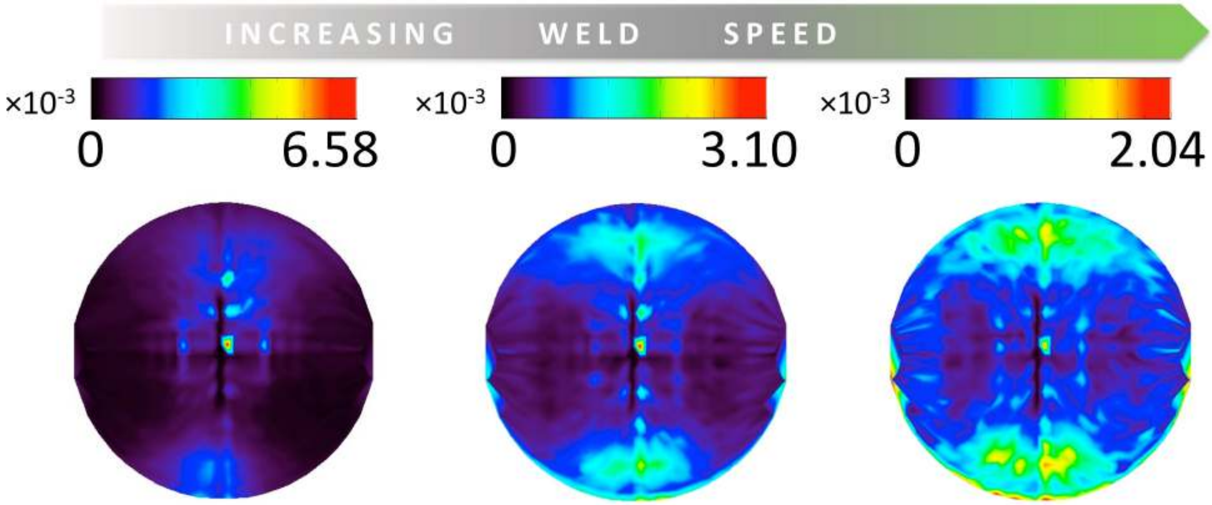

Figure 16 – Interfacial Normal Distribution Plots for 80 mm focal lens weld series machined at 1200 W delivered power for 1, 1.5, and 2m/min [40,m 60, 80 in/min]

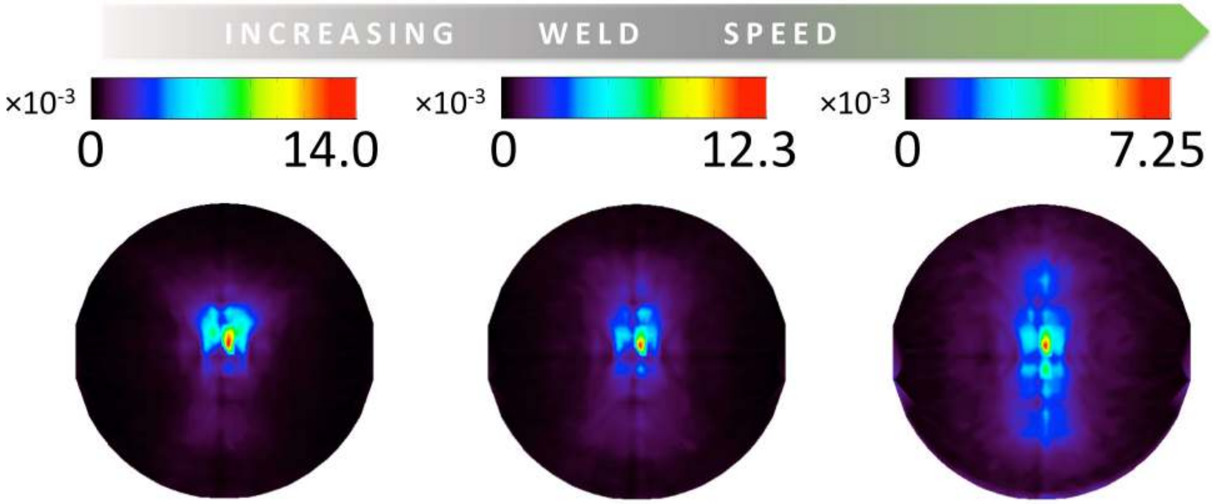

Figure 17 – interfacial Normal Distribution Plots for 120 mm focal lens weld series machined at 1200W delivered power for 1, 1.5, and 2 m/min [40, 60, 80 in/min]

4.3. Combined Metallographic + µCT Determinations

By combining metallographic observation with µCT observations, void volume fractions in each redundant weld were calculated, Table VI. Using the metallographic sections acquired, the cross-sectional area throughout the length of the weld can be approximated and compared to the directly measured porosity volumes. It should be mentioned; the uncertainty here is derived largely from the estimations of the total weld volumes, which were approximated by assuming a uniform cross-sectional area throughout the length of the weld based upon the observed metallographic cross-sections. The standard deviations reported in Table VI were calculated from the determined differences in weld volume estimated by using each of the three separate metallographic cross-sections. Porosity volume fraction was observed to yield a maximum of 8% ± 3.0 and a minimum of 1% ± 0.1 in the redundant welds examined, Figure 18 illustrates the trend and associated standard deviation.

Table VI – Weld Matrix with Calculated Porosity Volume Fractions

Focal Lens (mm)	Weld Speed (mm/min)	Porosity Volume Fraction
80	1016	0.079 ± 0.03
120	1016	0.081 ± 0.02
80	1524	0.017 ± 0.004
120	1524	0.023 ± 0.004
80	2032	0.009 ± 0.001
120	2032	0.014 ± 0.002

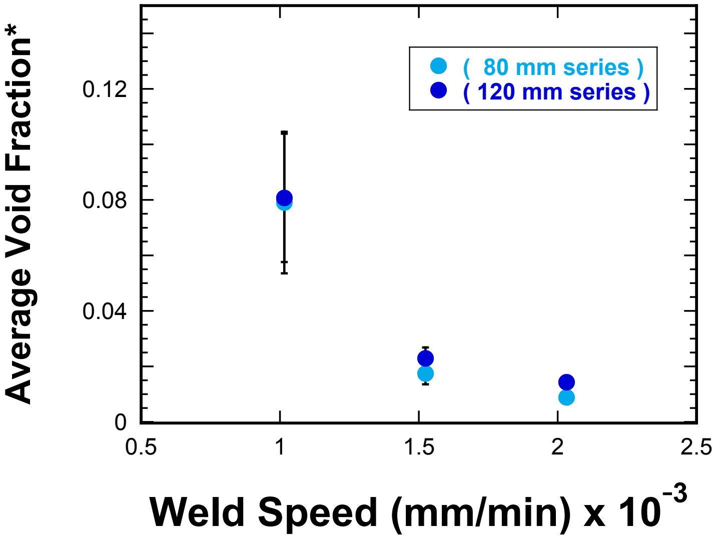

Figure 18 – Average Void Volume Fraction for welds created with 80 mm and 120 mm focal lens machined at 1200W delivered power at 1, 1.5, and 2 m/min [40, 60, 80 in/min]

4.4. Hardness, Calculated Tensile and Calculated Yield Strengths

Lastly, average Vickers hardness measures, calculated yield strengths (Y.S.) and calculated tensile strengths (T.S.) for both base metal (B.M.) and weld microstructures for all redundant samples are reported in Table VI below along with standard deviations for each measure.

Table VII – Vickers Hardness and Calculated Y.S. and T.S. for 1200W welds

Focal Lens (mm)	Weld Speed (mm/min)	B.M Vicker's Hardness (kg_f/mm^2)	Calculated Y.S. (MPa)	Calculated T.S. (MPa)	Weld Vicker's Hardness (kg_f/mm^2)	Calculated Y.S. (MPa)	Calculated T.S. (MPa)
80	1016	174	410 ± 17.0	550 ± 22.0	180	426 ± 45.0	571 ± 59.0
120	1016	174	408 ± 19.0	549 ± 24.0	176	415 ± 11.0	557 ± 14.0
80	1524	173	405 ± 16.0	544 ± 22.0	179	424 ± 19.0	569 ± 25.0
120	1524	169	395 ± 14.0	531 ± 18.0	177	418 ± 25.0	560 ± 32.0
80	2032	169	394 ± 13.0	530 ± 17.0	180	426 ± 18.0	572 ± 24.0
120	2032	169	396 ± 10.0	532 ± 13.0	174	410 ± 21.0	550 ± 27.0
--	--	166	386 ± 8.30	520 ± 11.0	--	--	--

Hardness measures reveal two important behaviors. First, for both focusing lenses examined, weld microstructures demonstrate increased hardness across all speeds compared to all base metal counterparts. Secondly, while no specific trends with regards to hardness were observed in the weldment alone, a trend towards a slight increase in hardness within the base metal is observed with decreasing weld speeds. This suggests that for this welding configuration, the base metal located away from the weld may have experienced similar microstructural strengthening as is occurring within the weld. The lower hardness exhibited at higher travel speeds is likely due to inadequate heat input needed to drastically affect the base metal. The fact that the hardness exhibited by the slow speed (e.g. 1016 mm/min) samples approach hardness levels exhibited by the welded regions themselves supports this assertion as greater heat input was provided to these samples. Furthermore, the hardness values for a sample of 304L base metal which has experienced no close or far-field welding environment (last line of Table VII) shows an average hardness measure slightly lower than the fastest speed welds further strengthening the argument for base metal strengthening with increasing exposure to heat or time during laser welding. To further illustrate the trending of material properties with weld speed and focusing lens, Figure 19 illustrates a suggested, calculated tensile strength using the micro-indentation measures and the relation of Eq. 2. It should be noted the calculated strength values are only an approximation for relative trending, not definitive individual measures.

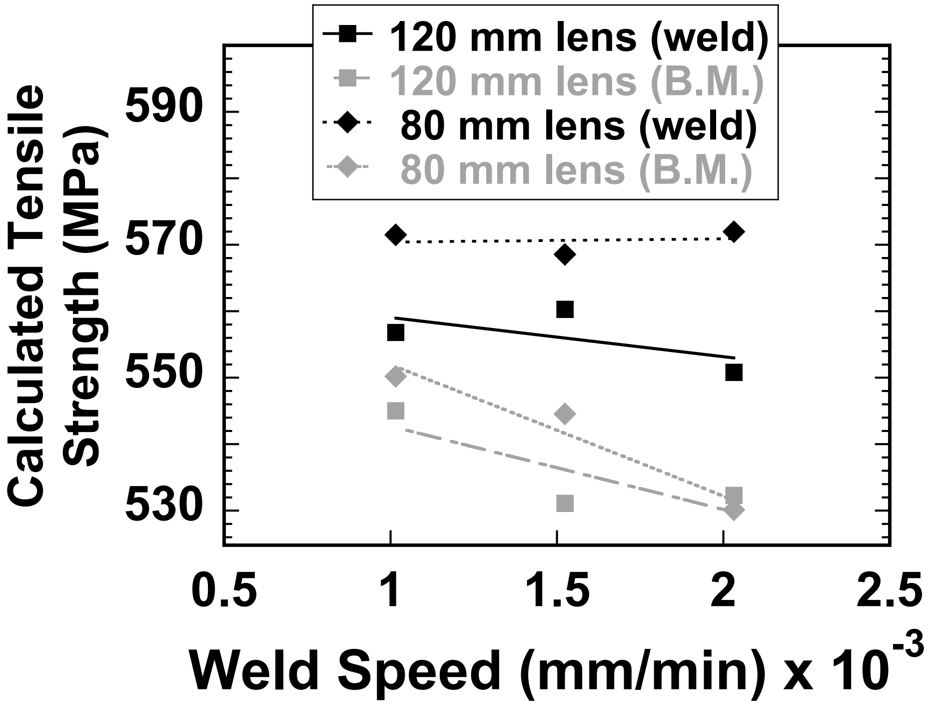

Figure 19 – Calculated Tensile Strength (MPa) from Vicker's Hardness Measures as a function of weld speed for both 80 mm and 120 mm focal lens series at 1, 1.5, and 2m/min [40,m 60, 80 in/min]

5. DISCUSSION

5.1. Implications to Prior Observations

As mentioned prior, specific understanding of the detailed microstructurally-influenced mechanical response of 304L following laser-welding is somewhat elusive. This work, however may provide some insight to earlier observations. In an effort to avoid the necessity of introducing various additional bodies of literature for consideration or assuming a familiarity of the reader with other works, the discussion presented here will be limited to the prior observations of the behavior of laser-welded 304L presented in section 2.1.2. Boyce, Reu and Robino[1] reported an increase in yield strength and extensive local ductility in the weld, but no substantial decrease in ultimate strength with the presence of porosity. This work certainly demonstrates agreement with the findings of a local increase in hardness and yield strength in the weldment. However, the work of Kuo and Jeng[18] clearly show changes in hardness in 304L accompanying increases in porosity content. The hardness measures of this work show minor changes as well with porosity content but no definitive trending over the small sample set investigated. However the hardness measures reported here do show a clear increase in hardness in the weld material as compared to the base material regardless of porosity content. The absence of definitive trending in the weld material is likely due to increasing inhomogeneity in the weld subsurface with increasing amounts of smaller pores as were identified by μCT. Furthermore, this inhomogeneity likely affects the clear trending of mechanical tensile strength and elongation in samples of 304L as shown in the experimental work of Boyce et al. as porosity was indeed found in the CW samples of Boyce and co-workers where none were previously identified due to resolution limits available at the time of their study. Furthermore, while extensive ductility has been observed in the weldment during mechanical tensile tests, the findings of increased hardness in the weld irrespective of porosity content suggests a concomitant effect of hardening in the weld material with increased ductility due to porosity content. These two competing effects may likely be the cause of a net-zero-change observation over the weld schedules often employed and altered in minor ways. The variation of porosity and local weld hardening may not be experiencing independent variations allowing for isolated study.

5.2. Implications to Modeling

Since the ability to deliver high heat input over very small areas provides many opportunities for welding with little disturbance to surrounding material, it follows that the depth to width ratio, would serve as a fairly effective indicator of the *"key-hole"* strength present during processing. However, further documentation of the resultant weld envelope and fusion zone shape can offer insight into the physical welding process. Increasing surface width to depth width ratio, (SW/DW) Figure 6a, indicate that while the overall depth to width (D/W) ratio remains largely unchanged over the weld speeds examined, Table III, the relative breadth of the subsurface weld interior becomes smaller by a factor of 1.5 – 2× in comparison to the weld at its surface. This indicates a diminishing of "key-hole" behavior with higher travel speeds. While this is a generally understood behavior due to the transition from keyhole to near conduction mode welding at very high speeds or very low powers, here we document powers and speeds over which such a transition begins to occur and the relative extent to which the weld interior narrows in comparison to the weld surface. Additionally, increases in weld speed are accompanied by decreases in crown height. Over the parameters investigated, the crown height actually becomes negative at 1.5 and 2 m/min, indicating a depression at the center-line of the weld below the surface of the base metal. Significant efforts have been undertaken by other investigators to model weld pool dynamics and even relate molten fluid flow to the final microstructure. Among these efforts, the most developed of computational models have centered around interactions due to surface tension [9], resolving velocity and temperature fields [89,90] and/or combining energy balance with three-dimensional fluid flow models [12]. The observance of the transition to a recessed weld pool surface here is noteworthy as it clearly documents a specific set of processing parameters around which such an event occurs. Furthermore, the fact that 304L has a well documented and publicly available library of material properties [90-92] for both its molten and solid states increases the opportunity for the parameters above to be useful as an experimental validation for models seeking to identify fluid flow or surface tension inflection points as well as keyhole perturbation or collapse.

5.3. Implications to Weld Processing

The progression of void volumes and the increase in voids per unit length are consistent with the observations of Norris *et al.* and suggest that while keyhole collapse [14-17] is a likely explanation for the porosity seen at low speeds, a very different mechanism may be at play at higher speeds. The smaller pores found at higher speeds exhibit a stark contrast from slow speed pores in frequency, longitudinal distribution and lateral position atop and below one another throughout the weld centerline. The widely accepted keyhole collapse models do not predict or suggest void populations of this arrangement, quantity or placement. The fundamental benefit of this work to weld processing is the identification of process parameter thresholds for the appearance of porosity and the quantification of pores present at varied speed and power combinations.

5.4. Suggestions for Further Investigations

Shape anisotropy measures reported here indicate approximation of porosity in high power, millimeter-scale laser welds as spheres is somewhat inaccurate and purports that ellipses are a more precise morphology. While anisotropy slightly decreases with increasing speed, no parameter set yields average 1:1:1 aspect ratios for the redundant sample conditions detailed in this report Table V. This holds particular importance for mechanical response models seeking to understand weldment necking, crack growth or deformation while incorporating physical or idealized pore geometries. Additionally, given the loading direction, the effects of substituting a spherical pore in place of an ellipse can generate very different and fundamentally disparate behavior. For this reason, providing further detail on pore orientation and directionality are worthwhile future efforts. Furthermore, pore shapes documented here, indicate returning singular pore diameters may result in increased levels of inaccuracy for measures such as shape, size and volume fraction. While approximation of the entire weld envelope should be improved to further reduce uncertainty in volume fraction calculations, such an improvement will likely require destructive methods such as serial-sectioning or changes to processing parameters such as the use of much smaller heat inputs to reduce variation throughout the length of the weld.

6. CONCLUSIONS

In summary, the characterization detailed here provides an advance in the qualitative and quantitative understanding of millimeter-scale laser weld microstructures with a chief emphasis on porosity. It was found that both macro- and microstructural features demonstrate marked trends with increasing weld speed and varying focal lens under the same delivered power. Furthermore, fully quantitative measures of void porosity were returned using micro-computed tomography, which revealed that void volumes, frequency, shape and volume fraction all vary distinctly with changes to documented processing parameters. It was also shown that porosity shapes discovered in these microstructures are more accurately described as ellipses rather than spheres. Lastly, it was shown that welds demonstrated higher hardness values than all base metal counterparts surrounding the weld. Future work will focus on integrating the developed characterization framework of these experimentally derived microstructural features with simulation and modeling efforts to import key microstructural averages and feature distributions for micro- and macro-scale simulations of void interaction and mechanical response.

7. REFERENCES

[1] B. L. Boyce*, et al.*, *Metall. Mater. Trans. A*, 2006, vol. 37A pp. 2481-2492.
[2] A. Haboudou*, et al.*, *Mater. Sci. Eng. A*, 2003, vol. A363 pp. 40-52.
[3] W. D. Feist and G.-R. Tillack (1997). Ultrasonic Inspection of Pores in Electron Beam Welds 'given at' European-American Workshop Determination of Reliability and Validation Methods of NDE, Berlin, Germany, NDT.net.
[4] J. Jellison and M. J. Cieslak (1994). Laser Materials Processing at Sandia National Laboratories 'given at' Applications of Lasers and Electro-Optics, Orlando, FL.
[5] G. A. Knorovsky*, et al.* (1999). Analysis and Validation of Laser Spot Weld-Induced Distortions 'given at' International Conference on Lasers and Electron Optics, San Diego, CA.
[6] P. W. Fuerschbach and J. T. Norris, SAND2003-3490: Understanding Metal Vaporization from Laser Welding (2003), D. o. Energy; Sandia National Laboratories
[7] P. K. Notz*, et al.*, SAND2007-5870: Use of Aria to Simulate Laser Weld Pool Dynamics for Neutron Generator Production (2007), D. o. Energy; Sandia National Laboratories
[8] C. V. Robino*, et al.*, SAND2002-4014: Solidification Diagnostics for Joining and Microstructural Simulations (2002), D. o. Energy; Sandia National Laboratories
[9] V. V. Semak*, et al.*, *J. Phys. D: Appl. Phys.*, 2006, vol. 39 pp. 590-595.
[10] W. S. Winters*, et al.*, SAND2005-3000: Progress Report for the ASCI AD Resistance Weld Process Modeling Project AD2003-15 (2005), D. o. Energy; Sandia National Laboratories
[11] R. Fabbro and K. Chouf, *J. Appl. Phys.*, 2000, vol. 87 (9), pp. 4075-4083.
[12] R. Rai*, et al.*, *J. Phys. D: Appl. Phys.*, 2007, vol. 40 pp. 5753-5766.
[13] P. Solano and G. Negro, *J. Phys D: Appl. Phys.*, 1997, vol. 30 pp. 3216-3222.
[14] A. F. H. Kaplan*, et al.*, *J. Phys. D: Appl. Phys.*, 2002, vol. 35 pp. 1218-1228.
[15] J. Y. Lee*, et al.*, *J. Phys. D: Appl. Phys.*, 2002, vol. 35 pp. 1570-1576.
[16] A. Matsunawa*, et al.*, *J. Laser Apps.*, 1998, vol. 10 (6), pp. 247-254.
[17] S. Pang*, et al.*, *J. Phys. D: Appl. Phys.*, 2011, vol. 44 pp. 1-15.
[18] T. Y. Kuo and S. L. Jeng, *J. Phys. D: Appl. Phys.*, 2005, vol. 38 pp. 722-728.
[19] O. Kamiya*, et al.*, *J. Mater. Sci.*, 2002, vol. 37 pp. 2475-2481.
[20] X. Zhu*, et al.*, *Int. J. Fatigue*, 2006, vol. 28 pp. 1566-1571.
[21] W. L. Daugherty and G. R. Cannell, *Pract. Fail. Analysis*, 2003, vol. 3 (4), pp. 56-62.
[22] J. T. Norris*, et al.*, *Welding J.*, 2011, vol. 90 pp. 198-203.
[23] J. T. Norris*, et al.*, SAND2007-1051: Evaluation of Weld Porosity in Laser Beam Seam Welds: Optimizing Continuous Wave and Square Wave Modulated Processes (2007), D. o. Energy; Sandia National Laboratories
[24] M. A. Mangan*, et al.*, *J. Microsc.*, 1997, vol. 188 (1), pp. 36-41.
[25] M. A. Mangan and G. J. Shiflet, *Scripta Mater.*, 1997, vol. 37 (4), pp. 517-522.
[26] M. V. Kral*, et al.*, *Mater. Charac.*, 2000, vol. 45 pp. 17-23.
[27] M. V. Kral and G. Spanos, *Scripta Mater.*, 1997, vol. 36 (8), pp. 875-882.
[28] M. V. Kral and G. Spanos, *Acta Mater.*, 1999, vol. 47 (2), pp. 711-724.
[29] M. V. Kral and G. Spanos, *Metall. Mater. Trans. A*, 2005, vol. 36A (5), pp. 1199-1207.
[30] G. Spanos*, et al.*, *Metall. Mater. Trans. A*, 2005, vol. 36A pp. 1209-1218.
[31] J. Madison*, et al.* (2008). Characterization of Three-Dimensional Dendritic Structures in Nickel-Base Single Crystals for Investigation of Defect Formation 'given at' Superalloys 2008, Seven Springs, Champion, PA, TMS.
[32] J. Madison*, et al.*, *JOM*, 2008, vol. 60 pp. 26-30.

[33] B. Maruyama*, et al.*, *Scripta Mater.*, 2006, vol. 54 pp. 1709-1713.
[34] J. Spowart, *Scripta Mater.*, 2006, vol. 55 (1), pp. 5-10.
[35] J. E. Spowart, *JOM*, 2006, vol. 58 (12), pp. 29-33.
[36] J. E. Spowart*, et al.*, *JOM*, 2003, vol. pp. 35-37.
[37] UES (2012). "ROBO-MET.3D." from http://www.ues.com/content/robomet3d.
[38] N. Chawla*, et al.*, 2004, vol. 51 pp. 161-165.
[39] N. Chawla*, et al.*, 2006, vol. 54 pp. 1541-1548.
[40] A. C. Lewis and A. B. Geltmacher, *Scripta Mater.*, 2006, vol. 55 (1), pp. 81-85.
[41] A. C. Lewis*, et al.*, *JOM*, 2006, vol. 58 (12), pp. 52-56.
[42] D. J. Rowenhorst and A. C. Lewis, *JOM*, 2011, vol. 63 (3), pp. 53-57.
[43] D. J. Rowenhorst*, et al.* (2009). Grain Boundary Curvature Analysis of B-Grains in Ti-21S 'given at' Microscopy and Microanalysis, Richmond, Virginia, Cambridge University Press.
[44] G. Spanos*, et al.*, *MRS Bull.*, 2008, vol. 33 (6), pp. 597-602.
[45] M. D. Uchic*, et al.*, *Ultramicrosc.*, 2009, vol. 109 pp. 1229-1235.
[46] M. D. Uchic*, et al.* (2004). Augmenting the 3D Characterization Capability of the Dual Beam FIB-SEM 'given at' Microscopy and Microanalysis, Savannah, Georgia, Cambridge University Press.
[47] M. D. Uchic*, et al.*, *Scripta Mater.*, 2006, vol. 55 (1), pp. 23-28.
[48] Y. Amouyal and D. N. Seidman, *Acta Mater.*, 2011, vol. 59 pp. 6729-6742.
[49] D. Isheim*, et al.*, *Scripta Mater.*, 2006, vol. 55 (1), pp. 35-40.
[50] D. N. Seidman*, et al.*, *JOM*, 2006, vol. 58 (12), pp. 34-39.
[51] M. P. Echlin*, et al.*, *Adv. Mat.*, 2011, vol. 23 (20), pp. 2339-2342.
[52] M. P. Echlin*, et al.*, *Rev. Sci. Instr.*, 2012, vol. 83 pp. 023701-023701 - 023706.
[53] J. Baruchel*, et al.*, *Scripta Mater.*, 2006, vol. 55 (1), pp. 41-46.
[54] J.-Y. Buffiere*, et al.*, *MRS. Bull.*, 2008, vol. 33 (6), pp. 611-619.
[55] K. H. Khor*, et al.*, *Scripta Mater.*, 2006, vol. 55 (1), pp. 47-50.
[56] E. M. Lauridsen*, et al.*, *JOM*, 2006, vol. 58 (12), pp. 40-44.
[57] E. M. Lauridsen*, et al.*, *Scripta Mater.*, 2006, vol. 55 (1), pp. 51-56.
[58] D. Juul Jensen*, et al.*, *MRS Bull.*, 2008, vol. 33 (6), pp. 611-619.
[59] M. D. Uchic*, et al.*, *JOM*, 2011, vol. 63 (3), pp. 25-30.
[60] K. J. Batenburg*, et al.*, *Ultramicrosc.*, 2009, vol. 109 pp. 730-740.
[61]
[62] M. Comer*, et al.*, *JOM*, 2011, vol. 63 (7), pp. 55-57.
[63] A. Y. M. Ontman and G. J. Shiflet, *JOM*, 2011, vol. 63 (7), pp. 44-48.
[64] S. Wang*, et al.*, *JOM*, 2011, vol. 63 (7), pp. 49-51.
[65] I. Wolf*, et al.* (2003). Extension of 2D Segmentation Methods into 3D by Means of Coons-Patch Interpolation 'given at' Medical Imaging 2003, SPIE.
[66] K. Thornton and H. F. Poulsen, *MRS Bull.*, 2005, vol. 33 (6), pp. 587-595.
[67] J. Millan*, et al.*, *Steel Res. Intl.*, 2010, vol. 82 (2), pp. 137-145.
[68] M. D. Uchic*, et al.* (2005). Microstructural Characterization of Aerospace Materials via Serial Sectioning using the Dual Beam FIB-SEM 'given at' Microscopy and Microanalysis 2005, Honolulu, Hawaii, Cambridge University Press.
[69] G. Spanos and D. J. Rowenhorst (2005). Three Dimensional Analysis of Phase Transformations in Ferrous Alloys 'given at' Microscopy and Microanalysis 2005, Honolulu, Hawaii, Cambridge University Press.
[70] D. Bernard*, et al.*, *Mater. Sci. Eng. A*, 2005, vol. 392 (1-2), pp. 112-120.

[71] A. Borbely*, et al.*, *JOM*, 2011, vol. 63 (7), pp. 78-84.
[72] A. S. Birks*, et al.*, Ultrasonic Testing (Nondestructive Testing Handbook, 2nd, American Society for Nondestructive Testint, Columbus, OH, 1991
[73] E. J. Pavlina and C. J. Van Tyne, *J. Mat. Engrg. Perform.*, 2008, vol. 17 (6), pp. 888-893.
[74] FergusonMetals (2012). "Technical Data." 2012, from http://www.upmet.com/media/302-304-304l-305.pdf.
[75] S. Kuo, Welding Metallurgy, John Wiley & Sons, Inc., Hoboken, NJ, 2003
[76] J. C. Lippold and D. J. Kotecki, Welding Metallurgy and Weldability of Stainless Steels, John Wiley & Sons, Inc., Hoboken, NJ, 2005
[77] R. W. Messler Jr, Principles of Welding: Processes, Physics, Chemistry and Metallurgy, John Wiley & Sons, Inc., New York, NY, 1999
[78] J. T. Norris, M.S. Thesis, New Mexico Institute of Mining and Technology, 2010
[79] T. Webber*, et al.*, Laser Beam Welding, ASM International, Materials Park, OH, 2011, pp. 556-569.
[80] R. Mendoza*, et al.*, *Metall. Mater. Trans. A*, 2003, vol. 34A (3), pp. 481-489.
[81] D. Kammer*, et al.*, *Scripta. Mater.*, 2006, vol. 55 (1), pp. 17-22.
[82] D. Kammer and P. W. Voorhees, *Acta Mater.*, 2006, vol. 54 pp. 1549-1558.
[83] J. Alkemper and P. W. Voorhees, *Acta Mater.*, 2001, vol. 49 pp. 897-902.
[84] D. J. Rowenhorst*, et al.*, *Acta Mater.*, 2006, vol. 54 pp. 2027-2039.
[85] J. L. Fife and P. W. Voorhees, *Acta Mater.*, 2009, vol. 57 pp. 2418-2428.
[86] D. Kammer and P. W. Voorhees, *MRS Bull.*, 2008, vol. 33 (6), pp. 611-619.
[87] A. L. Genau*, et al.*, *Scripta Mater.*, 2009, vol. 60 pp. 301-304.
[88] D. Kammer, Ph.D. Thesis, Northwestern University, Evanston, IL, 2006
[89] X. He*, et al.*, *J. Phys. D: Appl. Phys.*, 2003, vol. 36 pp. 1388-1398.
[90] X. He*, et al.*, *J. Phys. D: Appl. Phys.*, 2006, vol. 39 pp. 525-534.
[91] R. Steiner, ASM Handbook, Vol. 1: Properties and Selection: Irons, Steels, and High Performance Alloys, ASM International, Materials Park, OH, 1990
[92] J. R. Davis, ASM Specialty Handbook: Stainless Steels, ASM International, Materials Park, OH, 1994

DISTRIBUTION

1 Larry K. Aagesen
University of Michigan
Materials Science & Engineering
2300 Hayward Street
Ann Arbor, MI 48109

1	MS0372	John M. Emery	Org. 1524
1	MS0557	Burke L. Kernen	Org. 1522
1	MS0557	Ciji L. Nelson	Org. 1522
1	MS0836	R. Allen Roach	Org. 1516
1	MS0885	Terrance L. Aselage	Org. 1810
1	MS0886	Alice C. Kilgo	Org. 1822
1	MS0886	Donald F. Susan	Org. 1831
1	MS0889	Corbett C. Battaile	Org. 1814
1	MS0889	Brad Boyce	Org. 1831
1	MS0889	Charles V. Robino	Org. 1831
1	MS0889	Danny O. MacCallum	Org. 1831
1	MS0889	Deidre Hirschfeld	Org. 1831
1	MS0889	Elizabeth M. Huffman	Org. 1822
1	MS0959	David P. Adams	Org. 1832
1	MS1411	Amy Cha-Tien Sun	Org. 1814
1	MS1452	Jerome T. Norris	Org. 2552
1	MS9042	James W. Foulk, III	Org. 8256

1	MS0899	Technical Library	Org. 9536 (electronic copy)
1	MS0359	D. Chavez, LDRD Office	Org. 1911

Sandia National Laboratories